# Influence of External Heat Sources on Volumetric Thermal Errors of Precision Machine Tools

Lingtao Weng[a], Weiguo Gao[a, *], Zhanshan Lv[b], Dawei Zhang[a, *], Teng Liu[c], Yu Wang[a], Xiangyang Qi[d], Yanling Tian[a, e]

a Key Laboratory of Mechanism Theory and Equipment Design of Ministry of Education, Tianjin University, Tianjin 300354, China

b.Sinochem Jilin Changshan Chemical CO.,LTD, Songyuan, Jilin 131199, China

c School of Mechanical Engineering, Hebei University of Technology, Tianjin 300130, China

d School of Mechanical Engineering, Tianjin Polytechnic University, Tianjin 300387, China

e School of Engineering, The University of Warwick, Coventry CV4 7AL, UK

* Corresponding author. Tel./fax: +86 22 27405561. E-mail addresses: gaowg@tju.edu.cn (W. Gao).
Tel./fax: +86 22 27405561. E-mail addresses: medzhang@tju.edu.cn (D. Zhang).

## Nomenclature

| | |
|---|---|
| HIS | internal heat source |
| EHS | external heat source |
| ECC | electronic control cabinet |
| HPS | hydraulic pump station |

## Abstract

Volumetric accuracy is susceptible to thermal gradient that caused by internal heat source (IHS) and external heat source (EHS). In this paper, a temperature-structure multi-step calculation method is presented to investigate the influences of EHSs on volumetric thermal errors. Simulations are computed to study the effects of different EHSs on a machine tool and series of validating experiments are carried out to verify the modeling method. The tool tip deviations that occur in both simulation and experiment by EHSs effects are showed in this paper. The test results in specific position and working condition revealed that EHSs contribute 53%, 21% and 68% of thermal deviations in X, Y and Z directions individually. Thus, it becomes fairly apparent that the EHS is an important factor which can significantly affect the volumetric accuracy.

The methods provided in this paper are valuable for machine tool designers to evaluate the EHS effects on volumetric thermal errors during designing process; furthermore, some insulating measures are suggested to improve the accuracy and accuracy stability of precision machine tools by reducing the EHS influences.

## Keywords

Thermal radiation, external heat source, precision machine tool, volumetric thermal error

## 1. Introduction

Thermal errors of machine tools are one of the main factors affecting CNC machine tool accuracy [1], which represent up to 70% of the total errors of machined pieces for precision machining, thereby this problem is the focus of recent research studies [2-4]. Generally, heat sources can be broadly divided into two parts, internal heat sources (IHSs) and external heat sources (EHSs). IHSs include all heat sources that are directly caused by machine tool, such as servosystem, spindle motor and cutting process, etc. EHSs are mainly attribute to the environment in which the machine tool is installed and they affect machine tool through convection and thermal radiation. Most of the studies focus on machine tool internal sources analysis [5-8] while studies concerning the influences of EHS on machine tools are

insufficient. However, the impacts of EHS are non-negligible, especially for thermal sensitive precision machine tools. Therefore, it is significant to investigate the influences of EHS on precision machine tools.

EHS mainly include ambient temperature, lamp, electronic control cabinet (ECC), hydraulic pump station (HPS), etc. Different from IHSs, EHSs affect machine tool temperature through convection and thermal radiation. Some researchers investigated the impacts of environment temperature perturbation on machine tools and established some thermal characteristic models. Zhang [9] proposed analytical approaches of time domain and frequency domain to analyze the influence of time-varying environment temperature on machine tool thermal error. For simplicity, author decomposed the machine tool into several units composed of relatively simple structures, then calculated the overall thermal error transfer function. However, thermal gradients result in machine tool non-linear structure deformation. Hence, the simplification in this paper is not suitable for precision machine tool thermal error modeling. Finite element analysis (FEA) is an efficient calculation method which is widely used in machine tool temperature and deformation prediction. Mian [10] studied the effect of ambiance temperature swings on machine tool deformation by FEA. The presented modeling methodology observably reduced the machine downtime required to establish the thermal response. Regrettably, other EHSs which affect machine tool through thermal radiation were leave out of the consideration. Tan [11] further studied the environment thermal hysteresis effects and brought up a time-varying analytical model between environment temperature and thermal error of large machine tools using Fourier synthesis, time series and the Newton cooling law. Further, the experiment verifies that the ambient temperature has a significant influence on heavy-duty machine tool. However, other EHSs impacts such as lamps, ECC, HPS have not been discussed. Based on fiber Bragg grating sensing technology, Huang [12] measured real-time temperature and deformation filed of a heavy-duty machine tool. Experiments results indicated that the surface temperature and spindle thermal error have a similar change trend following the ambient temperature. Since this paper is focused on measurement methodology, thermal error prediction method has not been presented. Glänzel [13] proposed a novel method to provide the heat transfer parameters quickly and efficiently for transient environmental conditions. Furthermore, the temperature and heat transfer coefficient of column and the velocity and temperature of surrounding air were simulated. However, the deformations of machine tool have not been calculated. In general, the impacts of ambient temperature on machine tools have been investigated in previous studies while other EHSs convection and thermal radiation effects on machine tools still lack of systematic studies.

However, it has been validated that convection and thermal radiation have significant impacts on objects temperature distribution [14-15]. Wang [16] investigated the effects of convection and radiation from a high-temperature source on the thermal environment in an industrial building. The influences of various surface emissivity, Grashof and Nusselt numbers on simulation results are discussed. Meng [17] further studied the effects of radiation on predictive accuracy in the numerical simulations of industrial buildings. Simulation results showed that the overall temperature had great difference between a pure convection model and the combined convection and radiation model. However, both papers have not studied the impacts of heat sources on other objects. Arslanoglu [18] investigated the effect of radiation heat flux from lights lamps on human thermal comfort by both experimental and theoretical approaches. In addition, Kalmár [19] found that mean radiant temperature has a parabolic variation with the room height and length, therefore for a room shape there is a certain height for which the mean radiant temperature is minimum. Unfortunately, these methodologies and conclusions could not be used in machine tools directly. Besides, the published papers still have not systematically investigated the impacts of EHSs thermal radiation on machine tools.

This section has illustrated the previous studies about environment temperature and thermal radiation impacts. In addition, the insufficient of the studies about EHSs effects on machine tools are highlighted.

Hence, the aim of this paper is to analyze the effects of EHS on machine tool. The thermal radiation analysis and modeling method are proposed in Section 2. Further, machine tool temperature field and

structure thermal deformation, the volumetric thermal error distribution under different single and combined EHS are discussed in Section 3. Modeling method and its predicting accuracy are verified by experiments in Section 4. Section 5 gives some conclusions and suggestions to improve machine tool accuracy and accuracy stability.

## 2. Thermal radiation analysis and modeling method

### 2.1 EHS induced thermal errors modeling

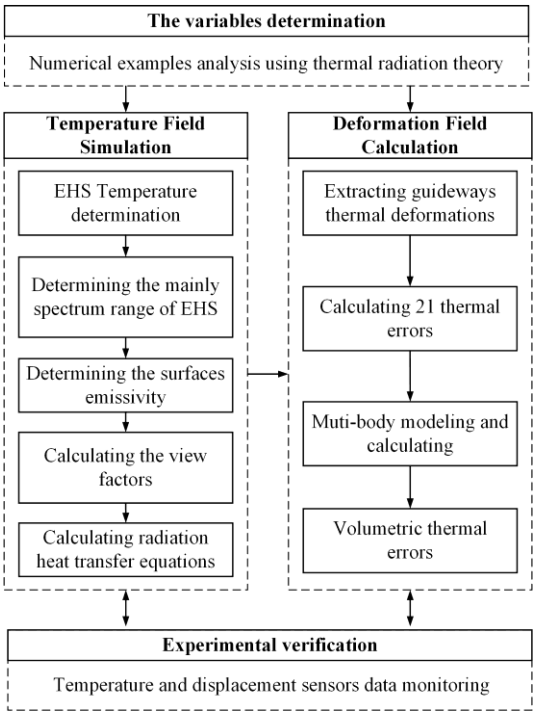


Fig. 1 Flowchart for temperature-structure multi-step calculation method

Machine tool temperature field and machining precision are affected by EHS through radiative heat transfer. In order to analyze the influences of EHS, this paper presented a temperature-structure multi-step calculation method based on finite element method, heat transfer theory and multi-body thermal error modeling theory. The temperature-structure multi-step calculation method mainly includes two parts, namely temperature simulation and deformation simulation, as given in Fig. 1. In order to investigate the effects of EHSs on machine tool, the study variables should be determined first. Some thermal radiation theories and a numerical case are therefore presented in section 2.2 to illustrate what and why we chose these variables as study objects.

Temperature simulation need to determine the thermal boundary conditions first, including EHS temperatures, spectrum ranges of EHSs, emissivity, etc. And the corresponding heat transfer between EHSs and a machine tool can be computed then. Since machine tool is a complicated mechanical system, it is hard to obtain the heats variations between EHS and the machine tool by analytical method. In order to facilitate the temperature and structural simulation analysis, Fluent and ANSYS are used to investigate the machine tool temperature and structure variations.

In addition, since it is time consuming for ANSYS to simulate the thermal deviations in whole working volume, the multi-body modeling method is proposed in section 2.4 to obtain the volumetric thermal errors. Furthermore, experiments are taken then to verify the results calculated in temperature-structure multi-step calculation method.

### 2.2 Theory analyses for the effects of key variables on radiative heat transfer

#### 2.2.1 Thermal radiation calculation process between two surfaces

Radiative heat transfer is an energy transfer process without medium participate, which is greatly different from heat conduction and thermal convection. For two surfaces $A_1$, $A_2$ as shown in Fig. 2, the

corresponding radiation energy transfer can be obtained by Stefan-Boltzmann and Lambert laws using:

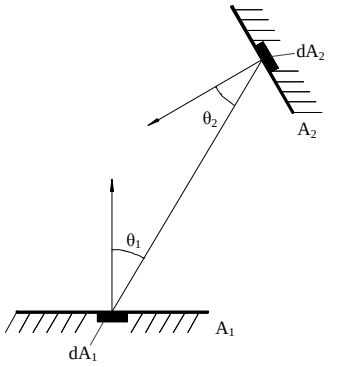


Fig. 2 Thermal radiation between surface $A_1$ and $A_2$

$$\Phi_{12} = \varepsilon_{\mathrm{f}} \mathrm{A}_1 \sigma \left[ \left( \frac{T_1}{100} \right)^4 - \left( \frac{T_2}{100} \right)^4 \right] X_{1-2} \tag{1}$$

where $\varepsilon_{\mathrm{f}}$ is the system emissivity, $A_1$ is the area of surface 1, $\sigma$=5.67 W/m$^2$•K$^4$ is the black body radiation coefficient, $T_{\mathrm{i}}$ is the temperature of surface *i* and $X_{\mathrm{i-j}}$ is the view factor from surface $A_{\mathrm{i}}$ to surface $A_{\mathrm{j}}$.

The value of $\varepsilon_{\mathrm{f}}$ is calculated as follows

$$\varepsilon_{\mathrm{f}} = \frac{1}{1 + X_{1-2}(1/\varepsilon_1 - 1) + X_{2-1}(1/\varepsilon_2 - 1)} \tag{2}$$

where $\varepsilon_i$ is the emissivity of surface *i*.

Parallel and vertical are two mainly spatial relationships between two surfaces. In practice, the view factors between surface $A_1$ and surface $A_2$ plotted in Fig. 3 (a) and (b) can be written in form Eq. (3) and Eq. (4) respectively.


(a) Parallel (b) Vertical

Fig. 3 Spatial relationship between $A_1$ to $A_2$

$$X_{1-2}^{p} = \frac{2}{\pi AB} \left\{ \begin{array}{l} \ln \left[ \frac{\left(1+A^2\right)\left(1+B^2\right)}{1+A^2+B^2} \right]^{1/2} + A\sqrt{1+B^2}\tan^{-1}\frac{A}{\sqrt{1+B^2}} \\ +B\sqrt{1+A^2}\tan^{-1}\frac{B}{\sqrt{1+B^2}} - A\tan^{-1}A - Y\tan^{-1}B \end{array} \right\} \tag{3}$$

$$X_{1-2}^{v} = \frac{2}{\pi D} \left\{ \begin{array}{l} W\tan^{-1}\frac{1}{D} + C\tan^{-1}\frac{1}{C} - (C^2+D^2)^{1/2}\tan^{-1}\frac{1}{(C^2+D^2)^{1/2}} \\ +\frac{1}{4}\ln\left\{ \frac{(1+C^2)(1+D^2)}{1+C^2+D^2} \left[ \frac{D^2(1+C^2+D^2)}{(1+C^2)(C^2+D^2)} \right]^{D^2} \left[ \frac{C^2(1+C^2+D^2)}{(1+D^2)(C^2+D^2)} \right]^{C^2} \right\} \end{array} \right\} \tag{4}$$

where $X_{1-2}^{p}$ is the view factor between two parallel surfaces, $X_{1-2}^{v}$ is the view factor between two

vertical surfaces, $L$ is the length of surface 1, $W$ is the width of surface 1, $H$ is the height of surface 2, $A$=$L$/$H$, $B$=$W$/$H$, C=$H$/$L$, $D$=$W$/$L$.

**2.2.2 Numerical comparison under different heat source temperature and distance**

According to Eq. (1) - (4), the radiative energy between surfaces $A_i$ and $A_j$ is mainly determined by $X_{i(j)-j(i)}$, $T_{i(j)}$ and $\varepsilon_f$ . For a given machine tool, the $\varepsilon_f$ is one of the material intrinsic property. However, the view factor $X_{i(j)-j(i)}$ is a variable parameter which is greatly depends on the distance $h$ between surface $i$ and surface $j$. In addition, the temperatures $T$ of EHSs are various and the effects of EHSs are different. In order to compare the effects of $h$ and $T$ and select the best study variables, numerical examples are calculated as follows.

An ideal constant temperature room model is presented in Fig. 4 (a). Since the lamps are mounted in the ceiling and generate heats, surface 1 is deemed as the heat source and the temperature of $T_t$ and the room height $H$ are chosen as variables. In order to illustrate the impacts of $T_t$ or $H$ on radiation heat transfer, the various net radiations of surfaces with different $T_t$ or $H$ are calculated in following numerical cases. The temperatures, emissivity and the sizes of surfaces in each case are listed in Table 1, where $T_s$ is the wall temperature, $\varepsilon_s$ is the wall emissivity.

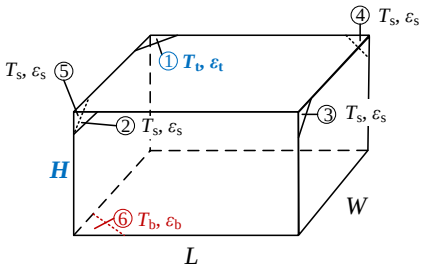


(a) Geometry model

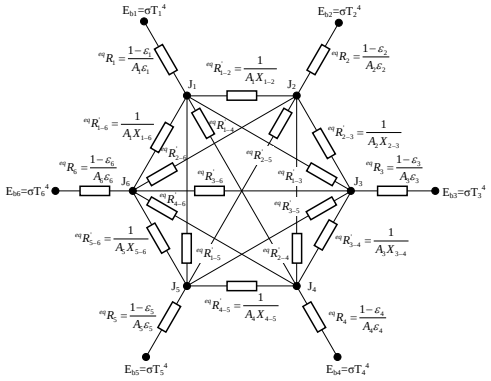

(b) Equivalent network

Fig. 4 Example model and equivalent network sketch

Table 1 Numerical calculation boundary condition

| | Constant Parameters | | | | | | | Variable | |
|---|---|---|---|---|---|---|---|---|---|
| | $T_s$ [℃] | $T_b$ [℃] | $\varepsilon_s$ | $\varepsilon_b$ | $\varepsilon_t$ | $L$ [m] | $W$ [m] | $T_t$ [℃] | $H$ [m] |
| Case 1 | 20 | 20 | 0.8 | 0.8 | 0.9 | 5 | 4 | **22** | **3** |
| Case 2 | 20 | 20 | 0.8 | 0.8 | 0.9 | 5 | 4 | **23** | **3** |
| Case 3 | 20 | 20 | 0.8 | 0.8 | 0.9 | 5 | 4 | **22** | **4** |

Take case 1 for example, the view factors matrix $X$ is determined using Eq. (3) and (4).

$$X=\begin{bmatrix} X_{1-1} & X_{1-2} & X_{1-3} & X_{1-4} & X_{1-5} & X_{1-6} \\ X_{2-1} & X_{2-2} & X_{2-3} & X_{2-4} & X_{2-5} & X_{2-6} \\ X_{3-1} & X_{3-2} & X_{3-3} & X_{3-4} & X_{3-5} & X_{3-6} \\ X_{4-1} & X_{4-2} & X_{4-3} & X_{4-4} & X_{4-5} & X_{4-6} \\ X_{5-1} & X_{5-2} & X_{5-3} & X_{5-4} & X_{5-5} & X_{5-6} \\ X_{6-1} & X_{6-2} & X_{6-3} & X_{6-4} & X_{6-5} & X_{6-6} \end{bmatrix}=\begin{bmatrix} 0 & 0.1910 & 0.1508 & 0.1910 & 0.1508 & 0.3163 \\ 0.2547 & 0 & 0.1522 & 0.1864 & 0.1522 & 0.2547 \\ 0.2514 & 0.1902 & 0 & 0.1902 & 0.1168 & 0.2514 \\ 0.2547 & 0.1864 & 0.1522 & 0 & 0.1522 & 0.2547 \\ 0.2514 & 0.1902 & 0.1168 & 0.1902 & 0 & 0.2514 \\ 0.3163 & 0.1910 & 0.1508 & 0.1910 & 0.1508 & 0 \end{bmatrix} \tag{5}$$

The net radiation of surface $i$ can be defined as Eq. (6) and network method of radiation heat exchange demonstrated in Fig. 4 (b) is used to calculate the net radiation $\Phi_i$ of each surface $i$. Besides, Kirchhoff's law is used to formulize the solving equations:

$$\Phi_i=\sum_{j=1,i\neq j}\Phi_{i,j} \tag{6}$$

$$-\frac{E_{bi}}{1-\varepsilon_i}+\sum_{j=1,j\neq i}^{6}X_{i-j}J_j=\frac{\varepsilon_i}{\varepsilon_i-1}E_{bi},(i=1,2,...,6) \tag{7}$$

Subsequently, the net radiation $\Phi_i$ can be obtained by Eq. (8), and the whole cases results are given in Table 2.

$$\Phi_i=\frac{(E_{bi}-J_i)\varepsilon_i A_i}{1-\varepsilon_i},(i=1,2,...,6) \tag{8}$$

Table 2 Net radiation $\Phi_i$ results

| | $\Phi_1$ [W] | $\Phi_2$ [W] | $\Phi_3$ [W] | $\Phi_4$ [W] | $\Phi_5$ [W] | $\Phi_6$ [W] |
|---|---|---|---|---|---|---|
| Case 1 | 196.2 | -38.9 | -30.0 | -38.9 | -30.0 | **-59.1** |
| Case 2 | 295.4 | -58.1 | -45.3 | -58.1 | -45.3 | **-89.5** |
| Case 3 | 198.7 | -31.4 | -25.4 | -31.4 | -25.4 | **-44.0** |

From Table 2, the net radiation $\Phi_i$ various with different $T_1$ and H. Take surface 6 as study object, $\Phi_6$ decreases 25% with H increases 1m and increases 51% with $T_1$ rises 1℃. The net radiation is enormously affected by the various distance and temperature. Therefore, the EHSs temperatures and the distances between EHSs and the machine tool are taken as key variable parameters in this paper. Furthermore, detailed simulations and calculations are implemented focus on the effects of these two parameters.

## 2.3 Structure deformation simulation and volumetric thermal error modeling

### 2.3.1 21 thermal errors calculating based on the guideways deformations

Multi-body method is a general error modeling method which is widely used in geometric volumetric error modeling [20-21]. The temperature-structure multi-step calculation method presented in this paper is based on this method and the mainly modeling process are as follows:

(1) Simulated the machine tool structure thermal deformations after the temperature field simulation.

(2) Extracted the guideways deformations from the structure deformation simulation results.

(3) Obtained the thermal deviations of reference coordinates of guideways.

(4) Calculated the 21 thermal errors based on guideways deformation.

(5) Calculated the volumetric thermal errors based on multi-body theory.

### 2.3.2 Thermal error modeling based on multi-body theory

Based on homogenous transformation matrices, multi-body theory can be used in machine tool error modeling from 21 thermal errors to volumetric errors. Fig. 5 exhibits the machine tool topological sketch and its kinetic model can be obtained by homogenous transformation matrices. Assuming the real tool point and the ideal tool point are defined as Eq. (8) and Eq. (9).

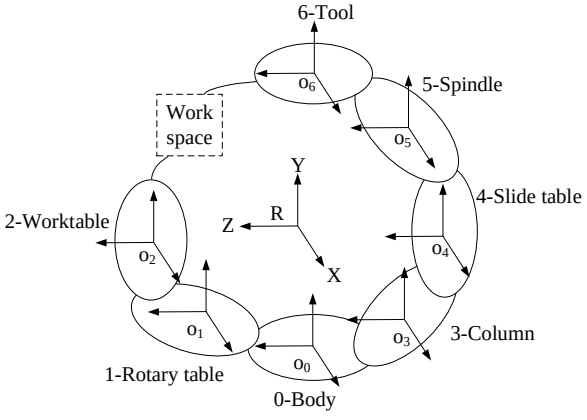


Fig. 5 Machine tool topology

$$P_t=[P_{tx},P_{ty},P_{tz},1]^{\mathrm{T}} \tag{8}$$

$$^{ideal}P_w=[^{ideal}P_{w,x},\ ^{ideal}P_{wy},\ ^{ideal}P_{wz},1]^{\mathrm{T}} \tag{9}$$

In the ideal machining situation, $\boldsymbol{T}_{b\text{-}t}P_t = \boldsymbol{T}_{b\text{-}w}\ ^{ideal}P_w$, where $\boldsymbol{T}_{b\text{-}t}$ is the transformation matrices from body to tool point, $\boldsymbol{T}_{b\text{-}w}$ is the transformation matrices from body to workpiece point. The transformation matrix from body *i* to adjacent body *j* has the matrix form Eq. (10).

$$\boldsymbol{T}_{ij}=\begin{bmatrix}1 & 0 & 0 & x\\ 0 & 1 & 0 & y\\ 0 & 0 & 1 & z\\ 0 & 0 & 0 & 1\end{bmatrix} \tag{10}$$

However, errors in real machining process are inevitable. Therefore, the relationship between real machining position and the ideal tool point is found out through the formula Eq. (11).

$$^{real}P_w=\left(^{e}\boldsymbol{T}_{b\text{-}w}\right)^{-1}\ ^{e}\boldsymbol{T}_{b\text{-}t}P_t \tag{11}$$

Where $^{e}\boldsymbol{T}_{b\text{-}w}$ and $^{e}\boldsymbol{T}_{b\text{-}t}$ can be derived from Eq. (12) and Eq. (13).

$$\begin{aligned}{}^{e}\boldsymbol{T}_{b\text{-}w} &= \prod_{bed}^{worlpiece}\boldsymbol{T}_{ij}^{p}\boldsymbol{\Delta T}_{ij}^{p}\boldsymbol{T}_{ij}^{s}\boldsymbol{\Delta T}_{ij}^{s}\\ &= \boldsymbol{T}_{01}^{p}\boldsymbol{\Delta T}_{01}^{p}\boldsymbol{T}_{01}^{s}\boldsymbol{\Delta T}_{01}^{s}\boldsymbol{T}_{12}^{p}\boldsymbol{\Delta T}_{12}^{p}\boldsymbol{T}_{12}^{s}\boldsymbol{\Delta T}_{12}^{s}\end{aligned} \tag{12}$$

$$\begin{aligned}{}^{e}\boldsymbol{T}_{b\text{-}t} &= \prod_{bed}^{Tool}\boldsymbol{T}_{ij}^{p}\boldsymbol{\Delta T}_{ij}^{p}\boldsymbol{T}_{ij}^{s}\boldsymbol{\Delta T}_{ij}^{s}\\ &= \boldsymbol{T}_{03}^{p}\boldsymbol{\Delta T}_{03}^{p}\boldsymbol{T}_{03}^{s}\boldsymbol{\Delta T}_{03}^{s}\boldsymbol{T}_{34}^{p}\boldsymbol{\Delta T}_{34}^{p}\boldsymbol{T}_{34}^{s}\boldsymbol{\Delta T}_{34}^{s}\boldsymbol{T}_{45}^{p}\boldsymbol{\Delta T}_{45}^{p}\boldsymbol{T}_{45}^{s}\boldsymbol{\Delta T}_{45}^{s}\boldsymbol{T}_{56}^{p}\boldsymbol{\Delta T}_{56}^{p}\boldsymbol{T}_{56}^{s}\boldsymbol{\Delta T}_{56}^{s}\end{aligned} \tag{13}$$

Where $\boldsymbol{T}_{ij}^{p}$ refers to ideal static homogenous transformation matrix, $\boldsymbol{T}_{ij}^{s}$ refers to the ideal motion homogenous transformation matrix, $\boldsymbol{\Delta T}_{ij}^{p}$ refers to the static error homogenous transformation matrix, $\boldsymbol{\Delta T}_{ij}^{s}$ refers to the motion error homogenous transformation matrix. And these homogenous transformation matrices can be calculated by Eq. (14).

$$\boldsymbol{\Delta T}_{ij}=\begin{bmatrix}1 & -\Delta\gamma & \Delta\beta & \Delta x\\ \Delta\gamma & 1 & -\Delta\alpha & \Delta y\\ -\Delta\beta & \Delta\alpha & 1 & \Delta z\\ 0 & 0 & 0 & 1\end{bmatrix} \tag{14}$$

And the final machining error $\Delta e$ is represented as follows

$$\Delta e = {}^{e}\boldsymbol{T}_{b\text{-}w}\ ^{ideal}P_w - {}^{e}\boldsymbol{T}_{b\text{-}t}P_t \tag{15}$$

## 3. Simulations and analyses of the effects of EHSs on a machine tool

Two CAD models were created with the same geometry and dimensions to simulate the temperature and structure simulation respectively (see Fig. 6 (b) and (c)). Fig. 6 (a) is a layout sketch of a constant temperature laboratory and the geometrical dimensions of EHS are presented in Table 3. Lamps and air inlets are mounted in ceiling, meanwhile, the air outlets are in the ground. The ECC and HPS are arranged around the machine tool. Fig. 6 (b) is a thermostatic room model used for CFD simulation. Fig. 6 (c) is a simplified model of JIG630 used for structural deformation simulation.

Steady-state pressure based solver was used for this simulation. Meanwhile, RNG $k-\varepsilon$ model was set for turbulence calculation, which is a kind of improved $k-\varepsilon$ model incorporated with eddy effects and provides dynamic Prandtl number calculation. Full buoyancy effects option and standard wall

functions of near-wall treatment were chosen in viscous model simulation.

Fluent provides five radiative calculation models like Rosseland model, P1 model, Discrete Transfer radiation model, Surface to Surface (S2S) model and Discrete Ordinates model. S2S model is easy to set up and has high calculation accuracy in the case where the medium does not participate in the radiation heat transfer. The air in constant temperature room can barely absorb or scatter radiative energy. Therefore, S2S model was used to calculate the thermal radiation simulation.

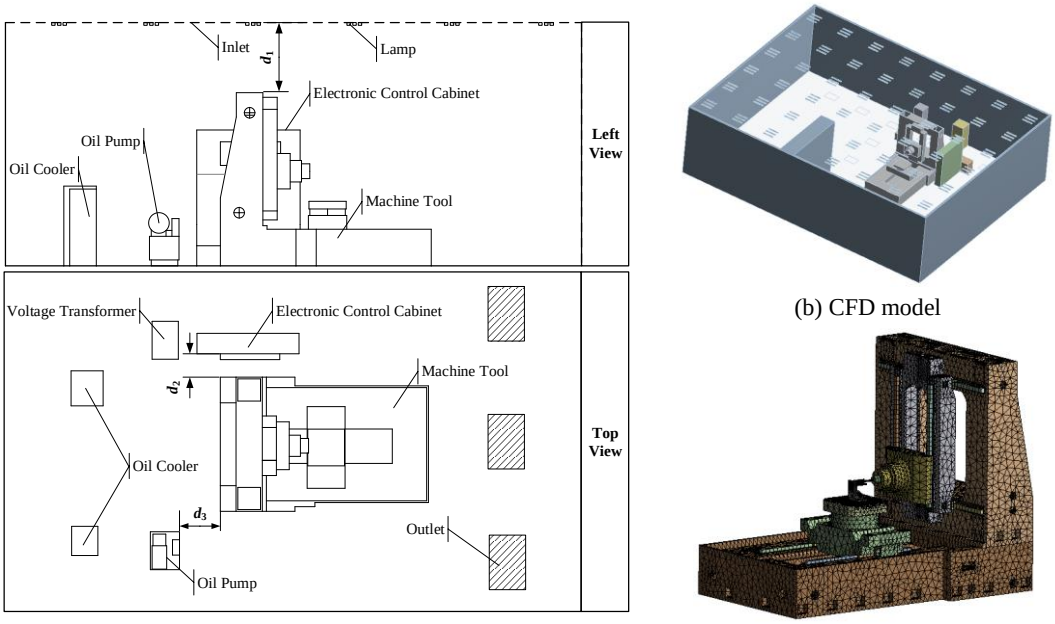


(a) Room layout schematic



(b) CFD model



(c) Machine tool model

Fig. 6 CAD models

Table 3 EHSs models geometrical dimensions

| EHS | Length [mm] | Width [mm] | Height [mm] | Diameter [mm] |
|---|---|---|---|---|
| ECC | 1750 | 350 | 2300 | / |
| Pump station pedestal | 700 | 600 | 500 | / |
| Oil pump | 500 | / | / | 300 |
| Lamp | 550 | / | / | 25 |

## 3.1 The simulated influences of single EHS on a machine tool

Lamp, ECC and pump station are three common EHSs. Furthermore, various EHSs temperatures $T_i$ and the distances $d_i$ shown in Fig.7 have different effects on machine tool. In order to clarify the influences of each EHS on a machine tool, detailed simulations are presented as follows and the CFD boundary conditions are listed in Table 4.

Table 4 CFD boundary conditions

| Inlet | | Wall | Air | |
|---|---|---|---|---|
| Temperature | Velocity | Heat transfer Coefficient | Density | Thermal expansion coefficient |
| [℃] | [m/s] | [w/m$^2$·℃] | [kg / m$^3$] | [1/℃] |
| 20 | 0.035 | 6 | 1.205 | 0.00366 |

### 3.1.1 Lamps radiation simulation

The temperature of lamps $T_1$ various with lamps type, brands, etc. Besides, the room height has diverse sizes in different factories. Therefore, simulations are computed with different $T_1$ and $d_1$. Fig. 7 (a) presents the machine tool temperature distribution of simulation case 1, meanwhile, the key boundary

conditions such as lamps temperature $T_1$, the distance between lamps and machine tool $d_1$, etc. are listed in Table 5. The lights can directly emit from lamps to the front side of bed or to the upper side of the column, which means the view factors between lamps to these regions are bigger thereby these regions are heating up obviously. Furthermore, the caused thermal gradient can lead the machine deforms as Fig. 7 (b).

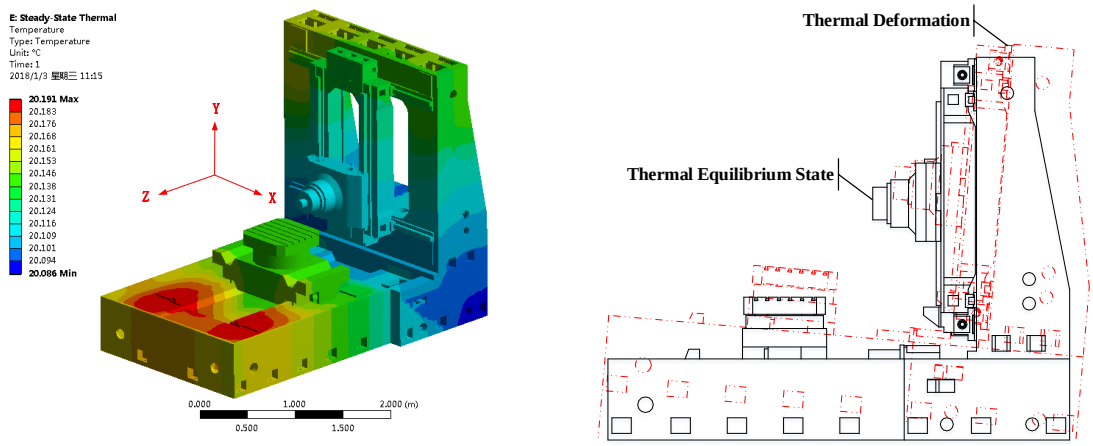


(a) Temperature field ($T_1$ is 31℃ and $d_1$ is 1000 mm) (b) Structure deformation schematic

Fig. 7 Machine tool temperature distribution and the structure deformation with lamp radiation

Table. 5 Boundary conditions of lamps simulation

| | Simulation case | 1 | 2 | 3 | 4 | 5 | 6 | 7 | 8 | 9 |
|---|---|---|---|---|---|---|---|---|---|---|
| Lamps | Temperature $T_1$ [℃] | **31** | **36** | **41** | **46** | **51** | 46 | 46 | 46 | 46 |
| | Distance $d_1$ [mm] | 1000 | 1000 | 1000 | 1000 | 1000 | **500** | **1500** | **2000** | **2500** |

Fig. 8 indicates the displacement variations of tool tip with various lamps temperatures $T_1$ and distances $d_1$. The increase of lamps temperature leads the tool tip leaning away from worktable in Z-direction. Further, the displacement in Z-direction increases about 0.7μm with the $T_1$ rises 5℃. Similarly, the relative displacement in Z-direction between worktable and tool tip decreases with the distance $d_1$ increases. And these variations mean that the column leans forward to worktable. However, due to the symmetrical structure of machine tool, the displacement barely changes in X and Y direction no matter $T_1$ increased or $d_1$ decreased.

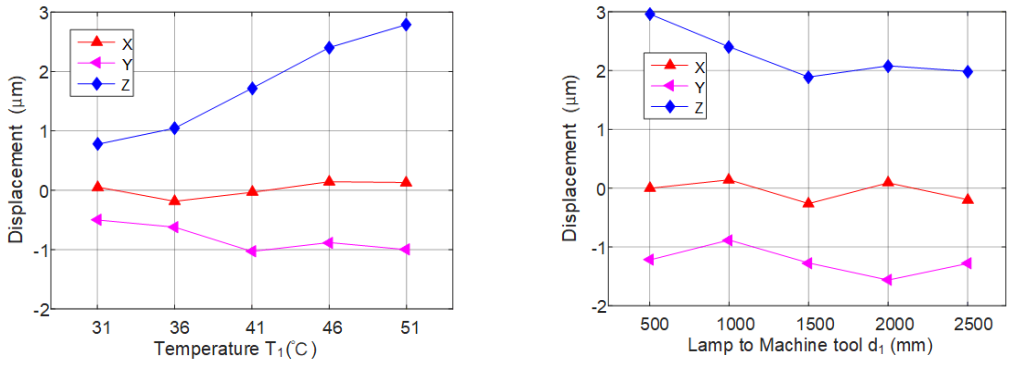


(a) Tool tip displacement with various $T_1$ ($d_1$ is 1000mm) (b) Tool tip displacement with various $d_1$ ($T_1$ is 46℃)

Fig. 8 Influence of lamp on tool tip displacement

### 3.1.2 ECC thermal radiation simulation

ECC temperature $T_2$ various with the different machine tool working condition changing and the distance $d_2$ between ECC to machine tool is easy to adjust. The influences of various $T_2$ and $d_2$ on machine

tool are simulated in this section. Fig. 9 (a) illustrates the machine tool temperature distribution caused by ECC and the key boundary conditions are listed in Table 6. On the whole, the temperature of machine tool surfaces that closer to ECC are higher than other sides, thereby the column leans away from ECC and deforms backward at the same time, as demonstrated in Fig. 9 (b).

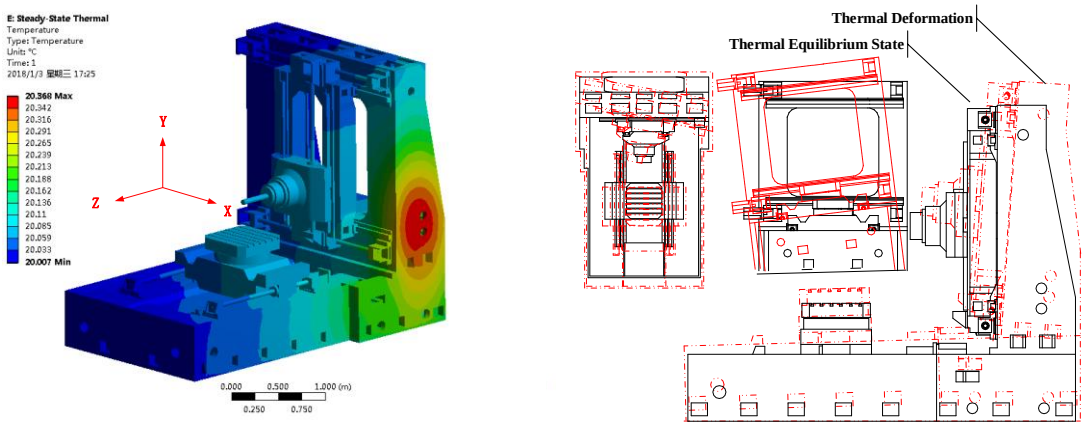


(a) Temperature field ($T_2$ is 21.3℃and $d_2$ is 450mm) (b) Structure deformation schematic

Fig. 9 Machine tool temperature distribution and the structure deformation with ECC radiation

Table. 6 Boundary conditions of ECC simulation

| | Simulation case | 1 | 2 | 3 | 4 | 5 | 6 | 7 | 8 | 9 |
|---|---|---|---|---|---|---|---|---|---|---|
| ECC | Temperature $T_2$ [℃] | **21.3** | **22.3** | **23.3** | **24.3** | **25.3** | 25.3 | 25.3 | 25.3 | 25.3 |
| | Distance $d_2$ [mm] | 450 | 450 | 450 | 450 | 450 | **250** | **350** | **550** | **650** |

Spindle rear deforms in all X, Y and Z directions obviously with the ECC average temperature $T_2$ rises as exhibited in Fig. 10 (a). According to Fig. 10 (b), the influences of increasing distance $d_2$ between ECC and machine tool on tool tip displacement are smaller. In other words, the $T_2$ rising 1℃has similar effects on the displacement of tool tip with the $d_2$ decreasing 200 mm. In addition, compare Fig. 10 with Fig. 8, the effects of distance $d_2$ decreases 100mm are similar to lamps temperature $T_1$ rises 10℃. Since $d_2$ is much smaller than $d_1$, the corresponding view factor of ECC $X_{ECC\_MT}$ is bigger than which of lamps $X_{Lamp\_MT}$. Thus, machine tool temperature field is much more sensitive with the variation of ECC temperature than lamps'.

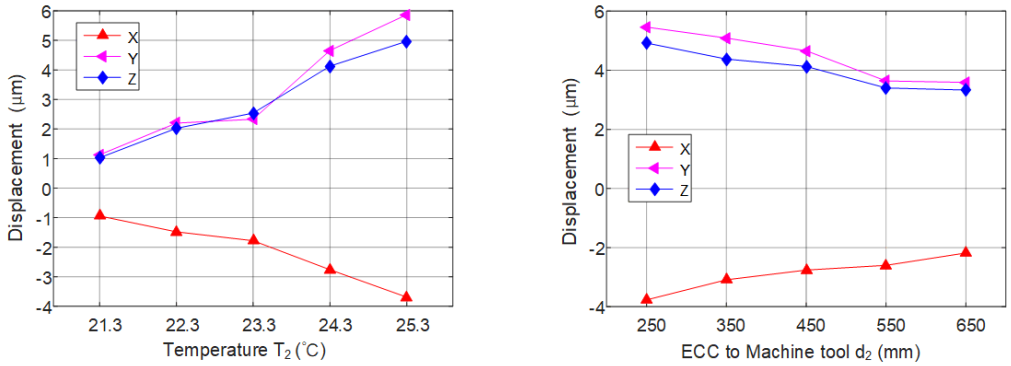


(a) Tool tip displacement with various $T_2$ ($d_2$ is 450 mm) (b) Tool tip displacement with various $d_2$ ($T_2$ is 25.3℃)

Fig. 10 Influence of ECC on tool tip displacement

### 3.1.3 HPS thermal radiation simulation

The effects of ECC and HPS are similar since the emissive power of both ECC and HPS are concentrated in infrared band (see Fig. 9 and Fig. 11). HPS mainly affects the left back side of machine tool because of the HPS installation location. Fig. 11 (b) shows the overall deformation tendency of the

machine tool under the influence of HPS. The column not only tilted forward worktable but also tilted away from the pump station.

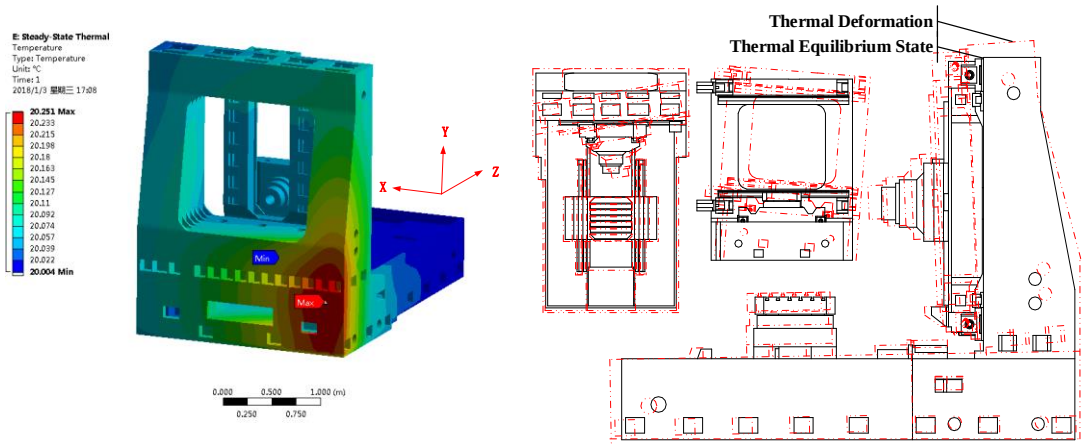


(a) Temperature field ($T_3$ is 32℃ and $d_3$ is 1050mm) (b) Structure deformation schematic

Fig. 11 Machine tool temperature distribution and the structure deformation with pump radiation

Table. 7 Boundary conditions of HPS simulation

| | Simulation case | 1 | 2 | 3 | 4 | 5 | 6 | 7 | 8 | 9 |
|---|---|---|---|---|---|---|---|---|---|---|
| **HPS** | **Temperature $T_3$ [℃]** | **32** | **35** | **38** | **41** | **44** | 38 | 38 | 38 | 38 |
| | **Distance $d_3$ [mm]** | 950 | 950 | 950 | 950 | 950 | **750** | **850** | **1050** | **1150** |

Fig.12 plotted the variation of tool tip displacement caused by diverse HPS temperatures $T_3$ and distances $d_3$. Relatively speaking, the variations of displacement in Y and Z direction are more obvious. Because of the Abbe effects, the displacement in X direction varies unapparent when spindle box is located in negative limitation position. However, displacement in X direction will be more noticeable when spindle box moved to positive limitation position. Besides, the displacement variation is more susceptible to the rising of temperature $T_3$ than decreasing of distance $d_3$.

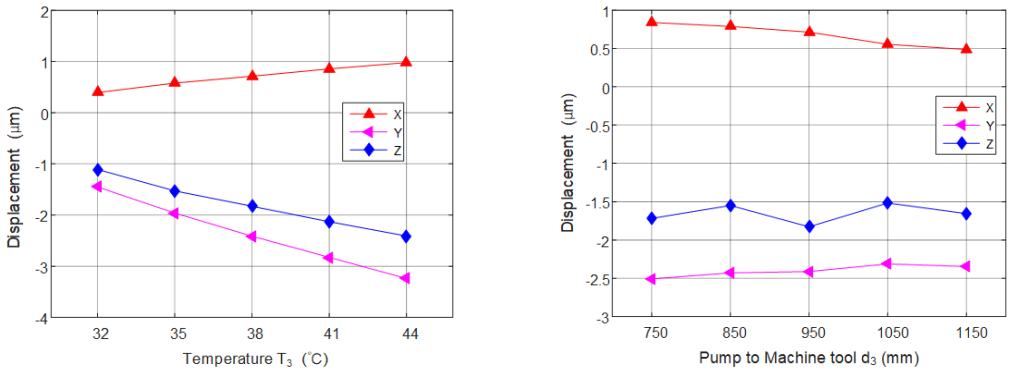


(a) Tool tip displacement with various $T_3$ ($d_3$ is 950 mm) (b) Tool tip displacement with various $d_3$ ($T_3$ is 38℃)

Fig. 12 Influence of pump station on tool tip displacement

## 3.2 The influences of synthetic external heat sources on workspace thermal errors

### 3.2.1 Temperature and structure deformation simulation

A synthetic calculation is carried out to analyze the impacts of comprehensive EHS on machine tool temperature field and volumetric thermal error. The CFD boundary conditions are same with Table 4 and the EHSs thermal conditions are listed in Table 8.

Table. 8 EHS thermal conditions

| | Lamps | ECC | HPS |
|---|---|---|---|
| Temperature [℃] | 31 | 21.5 | 32 |

According to Fig.13, the temperature distribution under synthetic EHSs effects is approximately equal to the superposition of each EHS. Further, the influences of lamps on machine tool are not so obvious as the effects of the ECC and HPS. The temperature of the back side of a machine tool is higher than that of other parts, since the ECC and HPS are arranged near the back of the machine tool.

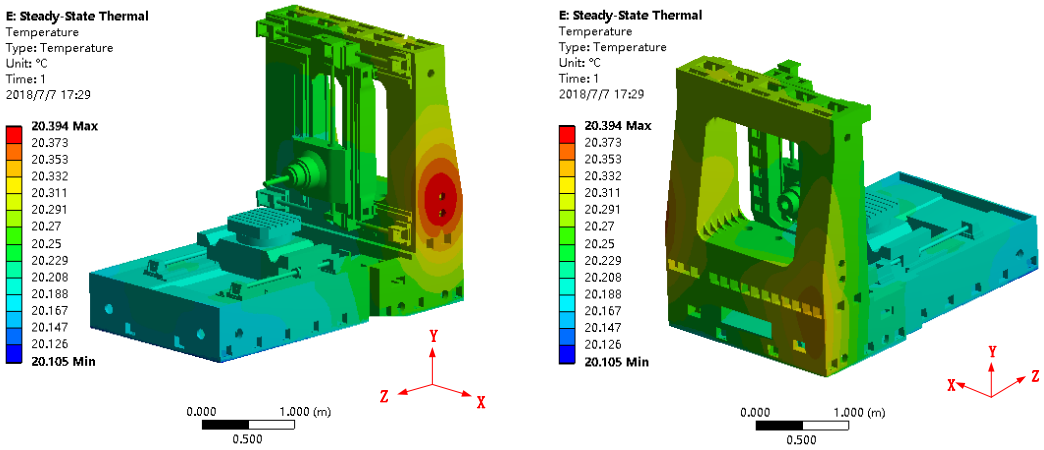


(a) Front side (b) Back side

Fig. 13 Machine tool temperature under comprehensive EHS influence

### 3.2.2 Volumetric thermal error calculation using multi-body method

Deformations of all guideways are extracted after ANSYS structural simulation. Subsequently linear and angular errors of each guideway and the volumetric thermal error can be calculated using multi-body method. According to ISO 230-6 [22], the working volume, three key paths $X_1X_2$, $Y_1Y_2$, $Z_1Z_2$ and two body diagonals *PPP* and *NPP* are defined in Fig. 14. In addition, the calculated 21 errors of machine tool are depicted in Fig. 15.

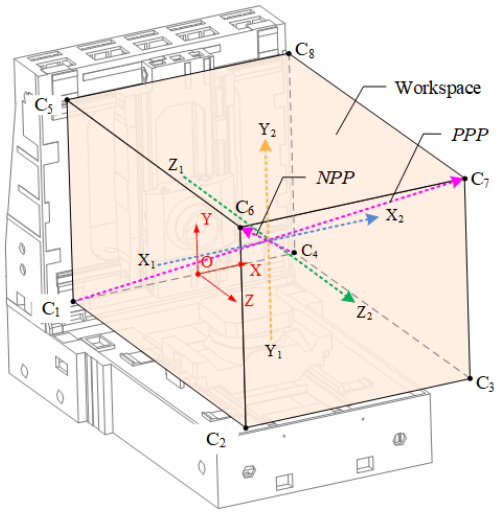


Fig. 14 Working volume and body diagonal

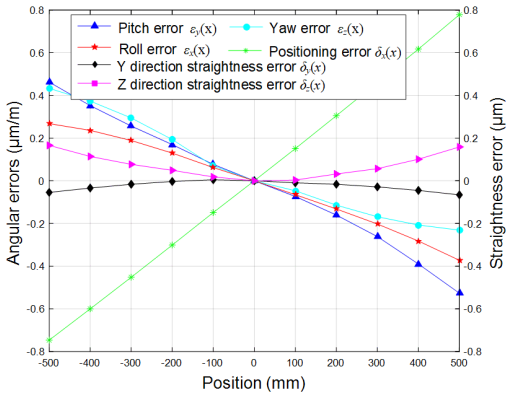


(a) Thermal errors of X axis guideway

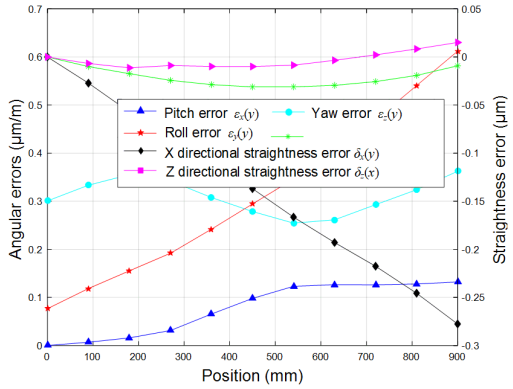


(b) Thermal errors of Y axis guideway

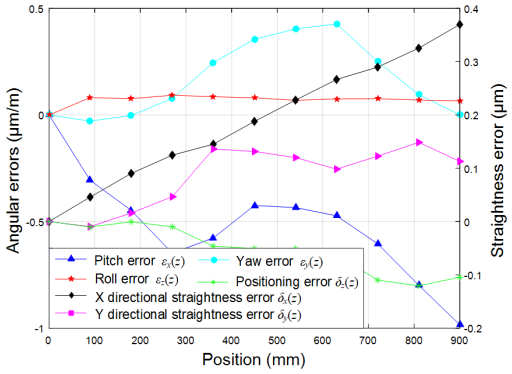


(c) Thermal errors of Z axis guideway

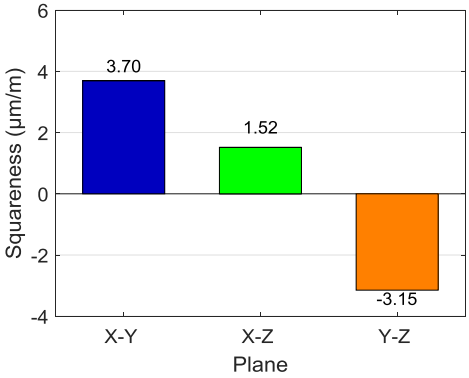


(d) Squareness errors

Fig. 15 21 thermal errors of machine tool

From demonstrated volumetric thermal error in Fig. 16, thermal errors in Y direction are relatively small, while errors in X and Z directions are larger. Since the column and bed are heated by EHSs at the same time, thermal expansions of these parts are generated simultaneously, thereby the relative displacement variation between tool tip and worktable in Y direction varied smaller than other two directions. Furthermore, the thermal error distribution in X direction is symmetric and it is caused by the layout of ECC and HPS around the machine tool. Observing Fig. 16 (d), the region with the largest overall thermal error is located at the positive limitation position of the X, Y and Z guideways.

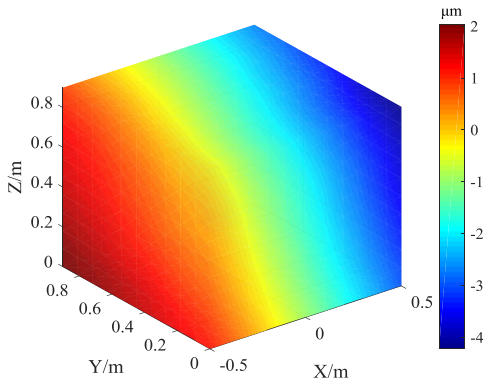


(a) X directional thermal error

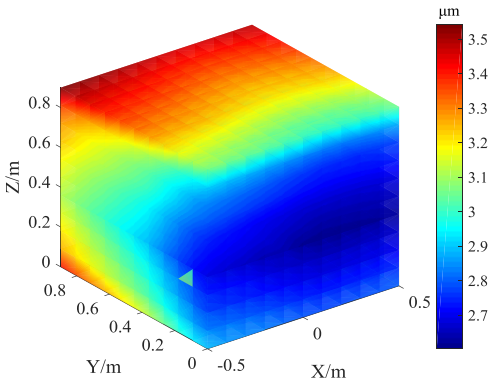


(b) Y directional thermal error

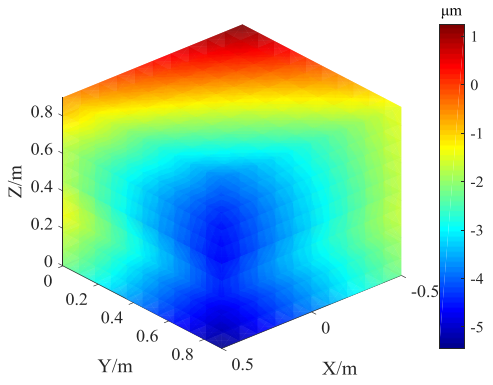


(c) Z directional thermal error

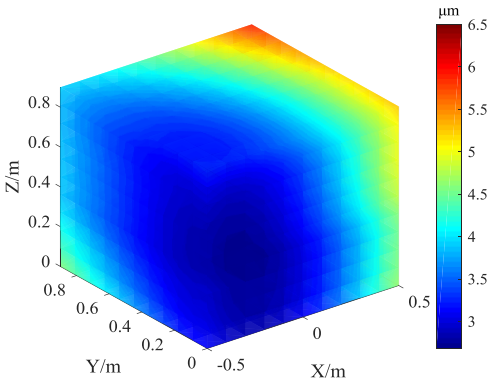


(d) Total thermal error

Fig. 16 Machine tool working volume thermal error under comprehensive EHS

Fig. 17 (a) – (c) show three directional thermal errors of paths $X_1X_2$, $Y_1Y_2$ and $Z_1Z_2$ which are defined in Fig. 14. The thermal errors in their length directions varied most obviously, while the variations of thermal errors in other two directions are smaller. According to Fig. 17 (d) and (e), the thermal errors curves of *NPP* and *PPP* are similar since the primary different of path *NPP* and *PPP* is the initial position of X axis. In addition, due to the Abbe effects, the thermal errors of both *NPP* and *PPP* gradually increase with the worktable moves along the positive direction of Y and Z guideways. Therefore, the maximum thermal error position is $C_7$ and the minimum thermal error position is point O. Specifically, the maximum total thermal error of working volume is 6.5μm and the minimum is 3μm.

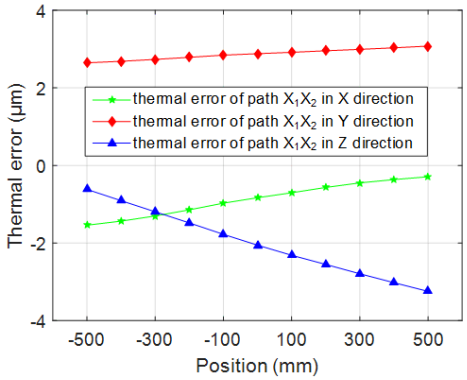


(a) Y and Z directional thermal error of path $X_1X_2$

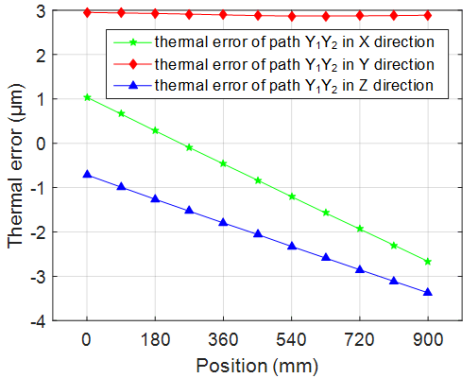


(b) X and Z directional thermal error of path $Y_1Y_2$

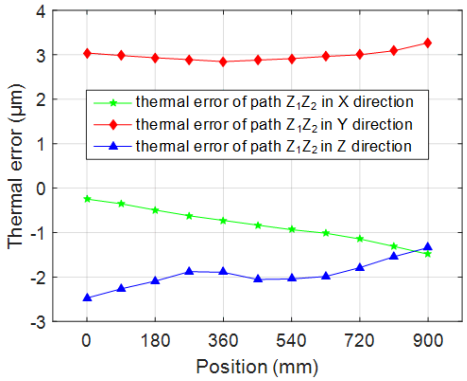


(c) X and Y directional thermal error of path $Z_1Z_2$

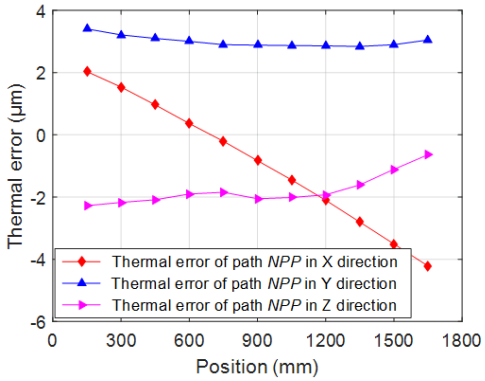


(d) *NPP* thermal error

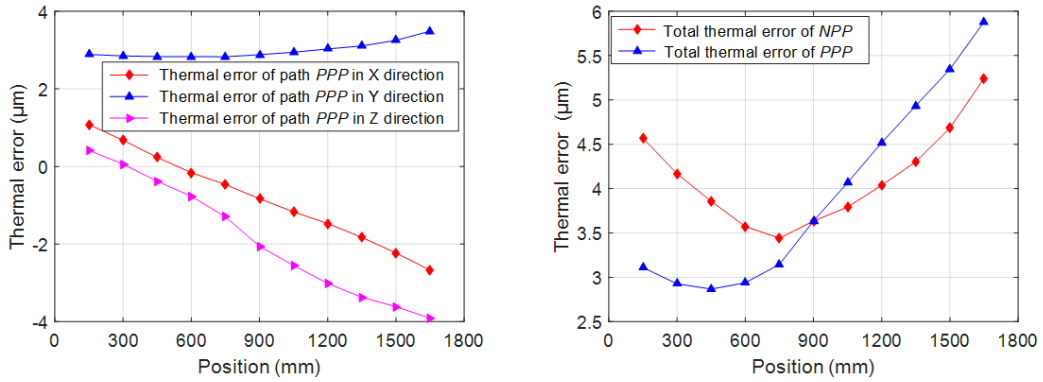


(e) *PPP* thermal error (f) Total thermal error of *NPP* and *PPP*

Fig. 17 Thermal errors in key paths

## 4. Experimental verification

### 4.1 Experimental setup and experiment process

The experimental tests were carried out on a JIG630 precision horizontal machine tool throughout different heat sources impacts in order to verify the proposed temperature-structure multi-step calculation method, and the experiment process is given in Fig. 18.

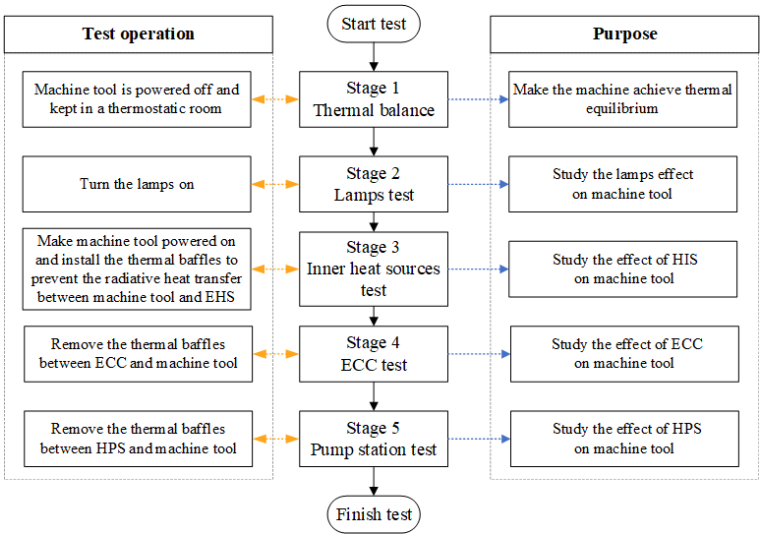


Fig. 18 Flowchart of experiment process

According to the principle of single variable, the experiment was divided into 5 stages and the influences of each heat source on the machine tool were investigated in different stages. Lamps thermal radiation experiment in stage 2 was implemented after machine tool thermal balanced in stage 1 to eliminate the influences of other heat sources. ECC and HPS barely generate heats if machine tool was powered off, the corresponding ECC and HPS experiments were therefore carried out after machine tool was powered on. In addition, since the ECC and HPS tests were taken after machine tool thermal rebalanced, thus the subsequent variations of sensors are caused by ECC or HPS individually. Furthermore, the operations in each stage in experiment are illustrated as follows.

(a) Stage 1 (0h – 18h): Thermal balance. Machine tool was powered off and kept in a thermostatic room to achieve its thermal equilibrium.

(b) Stage 2 (18h – 61h): Lamps test. Turned the lamps on to study the lamps effects on machine tool.

(c) Stage 3 (61h – 115h): Inner heat sources test. In order to minimal the interference of IHS on ECC and HPS tests results, the ECC and HPS experiments were taken after the machine was powered on and be thermal rebalanced. Meanwhile, thermal baffles were installed between EHSs and machine tool to

insulate EHSs thermal radiation. Besides, the thermal rebalance stage lasted for more than 2 days to ensure that machine tool was keeping in thermal equilibrium status.

(d) Stage 4 (115h – 139h): ECC test. The thermal baffles between ECC and machine tool were moved away, and the effects of ECC on the machine tool were investigated.

(e) Stage 5 (139h – 163h): HPS test. The thermal baffles between HPS and machine tool were moved away to study the HPS effects on machine tool.

The experimental setup is shown in Fig. 19. 27 PT100 temperature sensors with 0.01℃ resolutions were installed on the machine tool to collect the temperature variation, the installation locations and functions of sensors are shown in Table 9 and Fig. 20 (a) (b). Three non-contacting capacity displacement sensors with 9nm resolutions are installed on an invar holder to measure the displacements of a test bar as exhibited in Fig.19 and Fig. 20 (c). The X, Y, Z coordinates of the tested point are 500 mm, -840mm, -850mm. In addition, Table 10 listed the temperature of each EHS and the distance from EHS to machine tool.

Table 9 The installation locations and functions of sensors

| Sensor ID | Installation site | Function |
|---|---|---|
| T1, T2, T3, T4 | Column left/right side | Temperature measurement of column left/right |
| T5, T6, T7, T8 | Column rear | Temperature measurement of column rear |
| T9, T10 | Column top surface | Temperature measurement of column top surface |
| T11, T12 | Back side of bed | Temperature measurement of back side of bed |
| T13, T14, T15, T16 | Column front | Temperature measurement of column front side |
| T17, T18, T19, T20 | Bed upsides | Temperature measurement of bed upsides |
| T21, T22 | Environment | Environment temperature gradient measurement |
| T23 | Lamp | Temperature measurement of lamp |
| T24, T25, T26 | ECC | Temperature measurement of ECC |
| T27 | HPS | Temperature measurement of HPS |
| X, Y, Z | Test bar | Thermal deformation measurement of test bar |

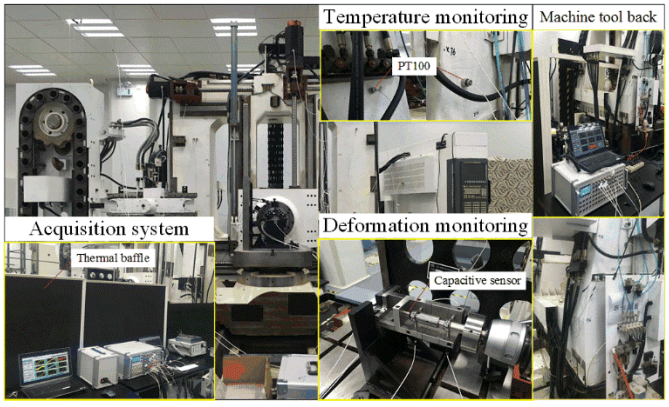


Fig. 19 The experimental precision machine tool

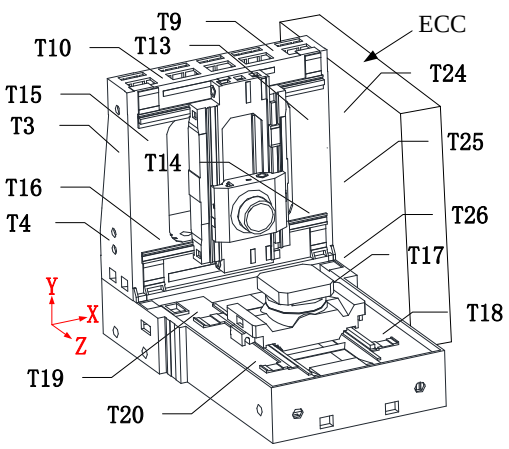


(a) Temperature sensors installed on the frontside

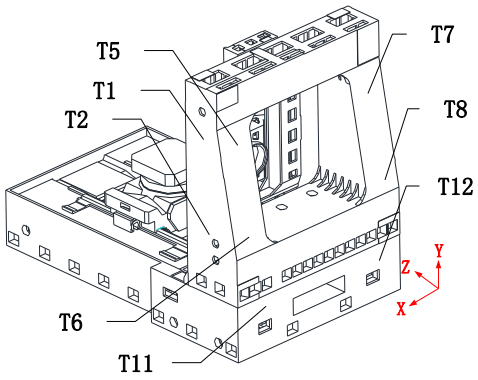


(b) Temperature sensors installed on the backside

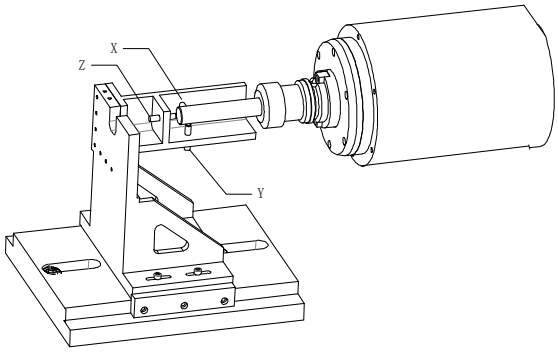


(c) Non-contact capacity displacement sensors

Fig. 20 Temperature and displacement points measured in the experiment

Table 10 EHS parameters conditions

| | **Lamp** | **ECC** | **Pump** |
|---|---|---|---|
| Average Temperature $T_i$ [℃] | 31 | 21.3 | 32 |
| Distance to machine tool $d_i$ [mm] | 970 | 400 | 1050 |

## 4.2 Experiments data analysis

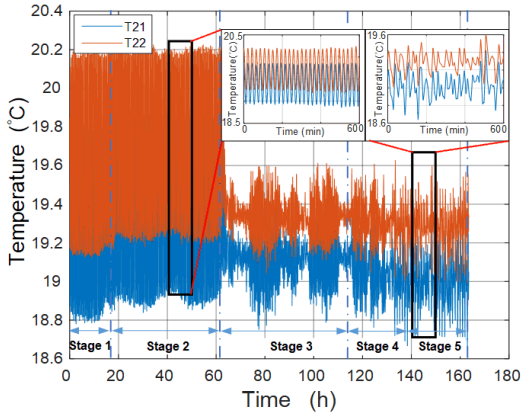


(a) Ambient air

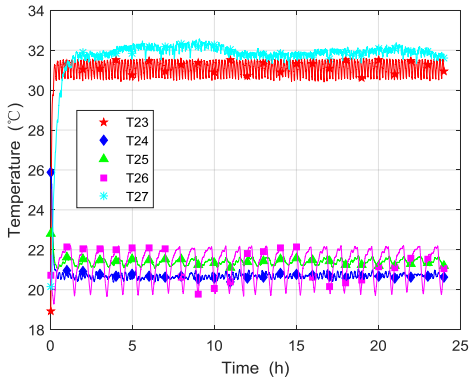


(b) Lamps, ECC and HPS

Fig. 21 EHSs temperatures

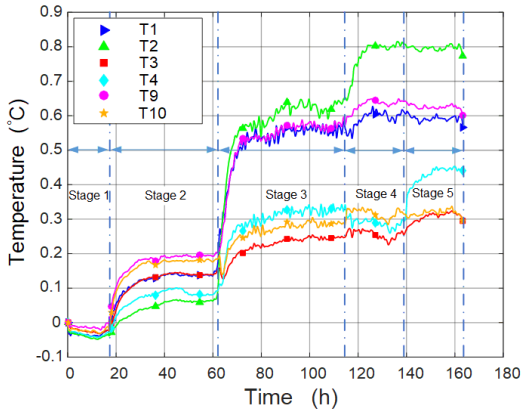


(a) Column left/right sides

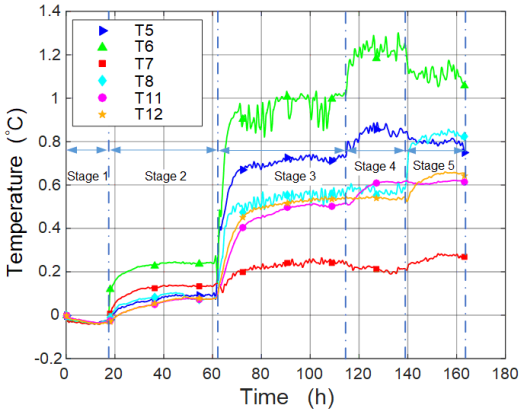


(b) Machine tool back sides

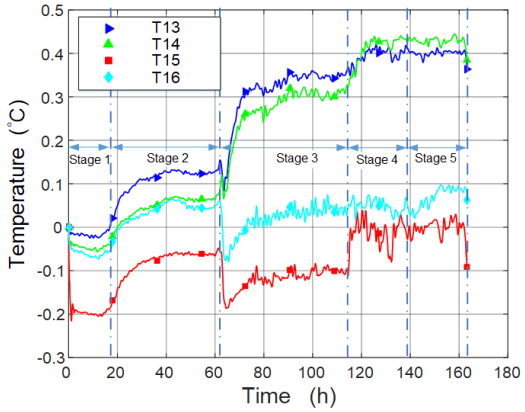


(c) Column front

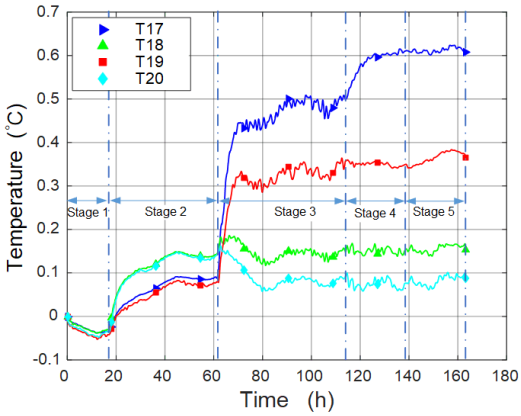


(d) Bed

Fig. 22 Measured temperature data

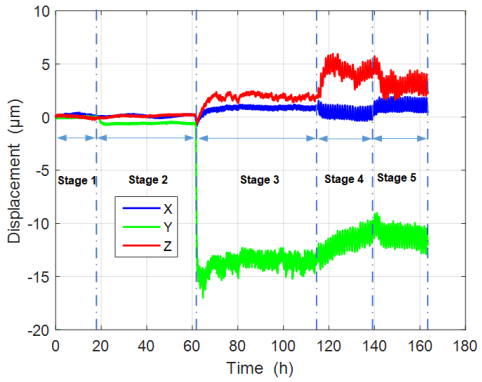


(a) Measured displacements during all experimental process

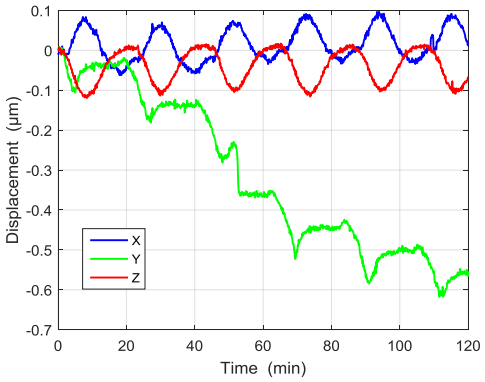


(b) Measured displacements in 120 min

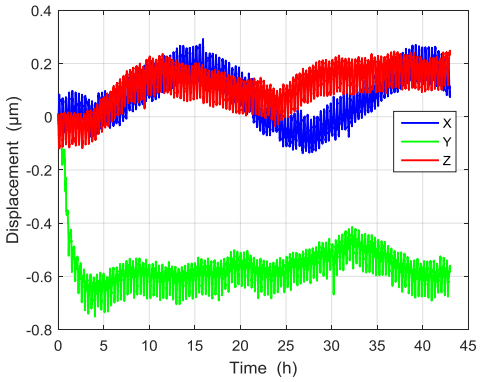


(c) Lamps caused displacements

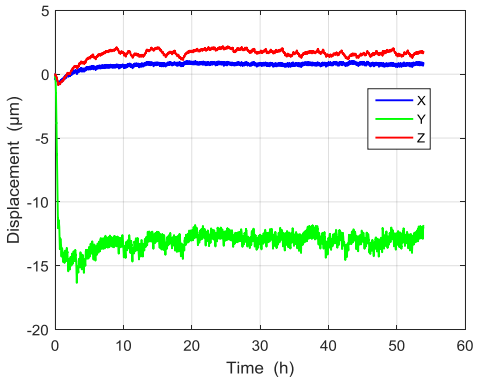


(d) IHS caused displacements

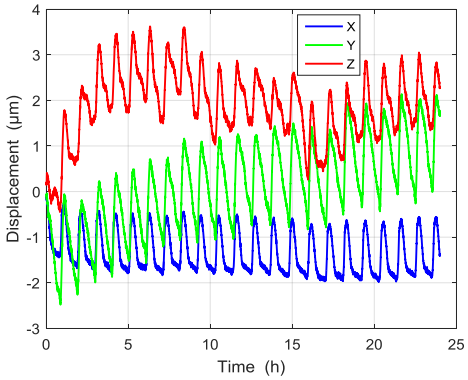


(e) ECC caused displacements

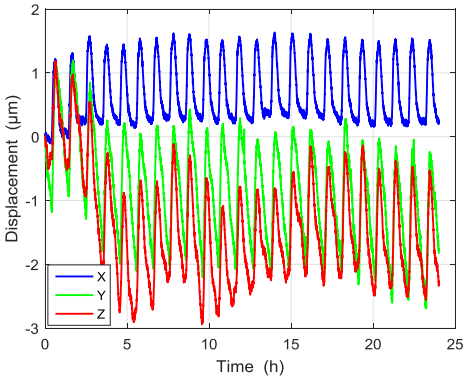


(f) HPS caused displacements

Fig. 23 Displacements between test bar and sensors

Table 11 displacement variation caused by different heat sources

| | Variation of displacement [μm] | | |
|---|---|---|---|
| **Heat source** | **X direction** | **Y direction** | **Z direction** |
| Lamp | 0.17 | -0.53 | 0.27 |
| IHS | 0.75 | -13.2 | 1.6 |
| ECC | -0.41 | 1.58 | 1.61 |
| HPS | 0.26 | -1.35 | -1.58 |

In order to ensure the machine tool was in thermal equilibrium status, an extra 18 hours monitoring test in stage 1 was carried out first. And the experiments under different thermal conditions were taken then. The temperatures of EHS are monitored as show in Fig.21. Fig. 22 and Fig. 23 shows the variations of filtered measured temperatures and displacements in different test stages and the detailed analysis are given as follows. For clarity, the various displacements caused by each EHS are listed in Table 11 and the corresponding pie charts are presented in Fig. 24. And the detailed discusses are proposed as follows.

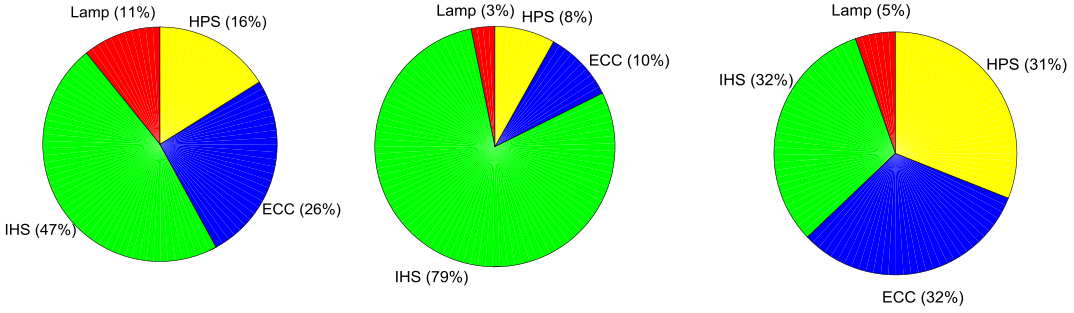

(a) X direction (b) Y direction (c) Z direction

Fig. 24 Different heat sources effects on measured displacements variation

(a). Analysis of lamps effects

The temperature of lamps is stable and fluctuate period is constant during whole test, as depicted in Fig. 21 (b). In addition, the fluctuating amplitude and cycle time of ambient air temperature are constantly no matter the lamps are turned on or off (see Fig. 21 (a)). In other words, the effects of lamps on thermostatic room ambient air temperature are not apparently, and the heat transfer between the machine tool and lamps are mainly through the way of thermal radiation. According to Fig. 22, the temperatures of column upper sides and the front of the bed raised 0.2℃ obviously. In addition, the temperatures of all monitoring points raised over than 0.1℃ which coincide with the simulation results computed in section 3.1.1. Furthermore, subsequent thermal gradients are generated and can result in structural deformations. Observing the results in Fig. 23 (c), the Y directional displacement decreases 0.53μm and Z directional displacement increases about 0.27μm. Fig. 23 (b) shows the monitoring displacements variation in 120min with lamps irradiation and the displacements show periodicity. Furthermore, it is worth noting that the period time of displacements fluctuation is consistent with the period time of temperature perturbation (see Fig. 21 (a)). Therefore, the ±0.5℃ variation of ambient temperature can cause ±0.06μm displacements swing.

(b). Analysis of IHS effects

The tests of ECC and HPS can only be implemented when the machine tool is turned on. Thus, the effects of IHS should be studied first. According to Fig. 22, after the machine tool is powered on, the temperatures of whole machine rising obviously, and the temperature increments are much bigger than other working conditions. These temperature variations are caused by the IHS including servo system, spindle motor, oil tubes, etc. Contrast with EHS, the impacts of IHS on the machine tool are more noticeable and faster. In addition, the displacement in Y direction varies markedly in test stage 3 and it takes about 10 hours to get a new thermal equilibrium status (see Fig. 23 (d)). Meanwhile, the fluctuate amplitude of ambient air temperature decreased to ±0.3℃ after machine tool is powered on, as shown in Fig. 21 (a). The following reason may contribute to this improvement. Additional heats are generated after the machine tool is powered on, thus improve the heating capacity of the laboratory and exactly meet the better air control system working condition.

(c). Analysis of ECC effects

ECC is one of the major EHSs and is installed close to the machine tool. From the monitoring results showed in Fig. 21 to Fig. 23, EHS has significant effects on machine tool temperature and structure deformation. The surfaces, with maximum rising temperature, are in the right sides of the machine tool. Further, the ECC mainly affect the machine tool surfaces near to ECC, while temperatures of other surfaces changed little. This dissymmetry temperature distribution could cause the column deformed in X direction. Fig. 23 (e) shows the displacement variations caused by ECC, with in X direction decreased about 0.41μm, Y direction increased 1.58μm and Z direction increased 1.61μm. Similar to Fig. 23 (b), the displacements changed periodically, however, the time period and amplitude are not the same. On one hand, the temperature of ECC changes periodically and the period time is familiar with that of displacements variation. On other hand, the displacement cyclical variation did not occur until the thermal baffles were moved away. Thus, the various temperature of ECC may contribute to the displacement fluctuate.

(d). Analysis of HPS effects

The effects of HPS on machine tool are similar with which of ECC. In stage 5, temperatures in some measured points raised about 0.22℃, while the temperatures of surfaces far from HPS barely

changed, as depicted in Fig. 22. Thermal gradient of the machine tool is generated due to this temperature variations, thereby deformed in X and Z directions. According to Fig. 23 (f), the displacements in X, Y and Z directions varied 0.26μm, -1.35μm and -1.58μm individually. Contrast with Fig. 23 (e), the displacements in three directions are opposite with each other and the following reasons may result these deformations. Firstly, the reversed displacements in X direction are caused by the layout of ECC and HPS around the machine tool. Secondly, the ECC mainly affects the right sides of the machine while the HPS mainly affects the left back sides of the machine tool, thereby the displacements in Y and Z directions are different.

## 4.3 Comparison of CFD simulations with experimental results

According to the comparisons in Fig. 25, the temperature simulations are more accurate than deformation simulations. Furthermore, the simulation results of lamps radiation have better accuracy than what of the ECC and HPS. The following reasons may take responsible for these deviations.

a) The boundary conditions are hard to set exactly due to the complex geometric surfaces of ECC and pump station.

b) Some sensors are affected by the cooling tubes and micro-electronic components which are hardly considered in simulation calculation.

c) The lack of sensors precision can also cause some errors.

The maximum predicted temperature errors of lamps, ECC and HPS are 0.03℃, 0.06℃ and 0.1℃ respectively. The differences of T2 and T6 in Fig. 25 (b) may be caused by mentioned reason c). According to the experiment photo showed in Fig. 19, the accuracies of T8 and T12 are under the influences of both aforementioned factors a) and b).

Besides, the displacements variations tendency of simulation and experiment are coincided, as shown in Fig. 25 (d). Due to the impacts of error average between mating parts and the aforementioned reasons, it is hard to achieve exactly forecast deformations. However, correct deformation tendency prediction is still a significant conclusion in thermal error compensation process.

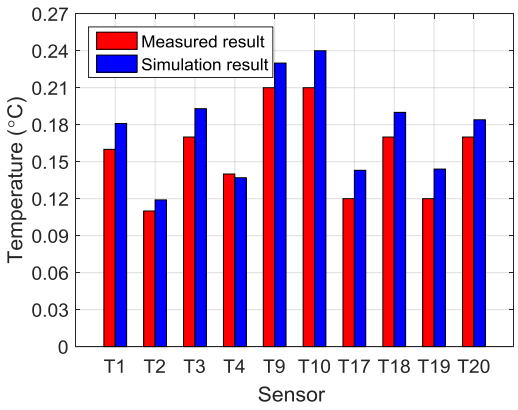


(a) Temperature of lamps experiment and simulation

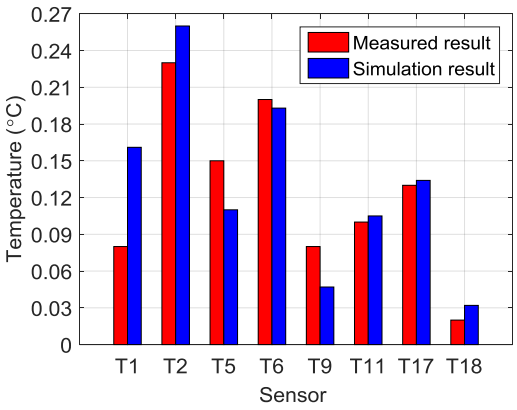


(b) Temperature of ECC experiment and simulation

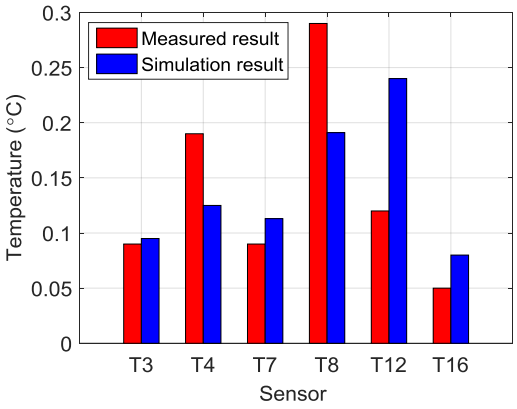


(c) Temperature of pump station experiment and simulation

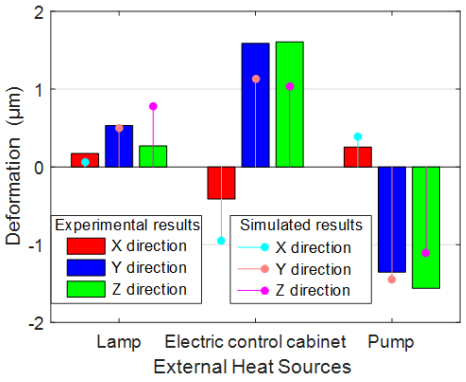


(d) Deformation of experiment and simulation

Fig. 25 Comparison between test and simulation

## 5. Conclusion

A temperature-structure multi-step calculation method, based on heat transfer theory, finite element method and multi-body thermal error modeling method, is proposed in this paper to evaluate the influences of EHS on volumetric thermal deviations of a machine tool. A series of simulations and validating experiments were carried out to obtain the effects of different EHSs on a machine tool. The temperature of an entire machine tool varied by lamps irradiation, while the ECC and HPS mainly affect the temperature distribution of a machine tool that close to them. Therefore, the cold light illuminator should be used instead of incandescent light bulb. It is also observed that the IHS contribute 47% to volumetric displacements variations in X direction and other EHSs contribute 53%. Furthermore, the effects of IHS, ECC and HPS on Z directional distortion are almost the same, and they contribute around 95% for total. In addition, the effects of IHS on a machine tool Y directional deformation are nearly 4 times bigger than which of EHSs.

Another interesting observation is that the machine tool is more sensitive to EHS temperature fluctuations than distance variations. Furthermore, the symmetrical layout of ECC and HPS can counteract the X directional thermal errors caused by each other. In order to minimize the effects of ECC and HPS on a machine tool, thermal baffles should be installed between ECC, HPS and the machine tool individually.

Proposed temperature-structure multi-step calculation method will assist the machine tool designers to evaluate the effects of EHS on machine tools and make machine tools reach higher levels of accuracy.

## Acknowledgments

The authors gratefully acknowledge the supports of National science and technology major project of China under Grant No.2015ZX04005-001, the fund of national nature science foundation of china No.51775375, the fund of nature science foundation of Tianjin No. 17JCZDJC40300, the Youth Talent Program of Higher Education Institutions in Hebei Province of China (BJ2017039) and the Youth Project of Natural Science Foundation in Hebei Province of China (E2017202194);We also thank for the reviewers' comments.

## References

1. Miao EM, Gong YY, Dang LC, Miao JC (2014) Temperature-sensitive point selection of thermal error model of CNC machining center. Int J Adv Manuf Technol 74: 681-691
2. Wang LP, Wang HT, Li TM, Li FC (2015) A hybrid thermal error modeling method of heavy

machine tools in z-axis. Int J Adv Manuf Technol 80: 389–400
3. Bryan JB (1990) International status of thermal error research. Ann CIRP 39(2):645–656
4. Shi H, Zhang DS, Yang J, Ma C, Mei XS, Gong GF (2016) Experiment-based thermal error modeling method for dual ball screw feed system of precision machine tool. Int J Adv Manuf Technol 82: 1693-1705
5. Liu T, Gao WG, Tian YL, Mao K, Pan GX, Zhang DW (2015) Thermal simulation modeling of a hydrostatic machine feed platform. Int J Adv Manuf Technol 79: 1581-1595
6. Liu T, Gao WG, Tian YL, Zhang HJ, Chang WF, Mao K, Zhang DW (2015) A differentiated multi-loops bath recirculation system for precision machine tools. Appl Therm Eng 76: 54-63
7. Du ZC, Yao XD, Hou HF, Yang JG (2018) A fast way to determine temperature sensor locations in thermal error compensation. Int J Adv Manuf Technol 97: 455-465
8. Jin C, Wu B, Hu YM (2015) Temperature distribution and thermal error prediction of a CNC feed system under varying operating conditions. Int J Adv Manuf Technol 77: 1979-1992
9. Zhang CX, Gao F, Li Y (2017) Thermal error characteristic analysis and modeling for machine tools due to time-varying environmental temperature. Precis Eng 47: 231-238
10. Mian N.S, Fletcher S, Longstaff A.P, Myers A (2013) Efficient estimation by FEA of machine tool distortion due to environmental temperature perturbations. Precis Eng 37: 372-379
11. Tan B, Mao XY, Liu HQ, Li B, He SP, Peng FY, Yin L (2014) A thermal error model for large machine tools that considers environmental thermal hysteresis effects. Int J Mach Tools Manuf 82–83: 11-20
12. Huang J, Zhou ZD, Liu MY, Zhang EL, Chen M, Pham D.T, Ji CQ (2015) Real-time measurement of temperature field in heavy-duty machine tools using fiber Bragg grating sensors and analysis of thermal shift errors. Mechatronics 31: 16-21
13. Glänzel J, Ihlenfeldt S, Naumann CC, Matthias P (2017) Decoupling of Fluid and Thermo-elastic Simulations on Machine tools Using Characteristic Diagrams[J]. Proc CIRP, 62:340-345
14. Nouanegue H, Muftuoglu A, Bilgen E (2008) Conjugate heat transfer by natural convection, conduction and radiation in open cavities. Int J Heat Mass Tran 51: 6054-6062
15. Sharma AK, Velusamy K, Balaji C, Venkateshan S.P (2008) Conjugate turbulent natural convection with surface radiation in air filled rectangular enclosures. Int J Heat Mass Tran 50: 625-639
16. Wang Y, Meng XJ, Yang XN, Liu JP (2016) Influence of convection and radiation on the thermal environment in an industrial building with buoyancy-driven natural ventilation. Energ Buildings 75: 394-401
17. Meng XJ, Wang Y, Liu TN, Xing X, Cao YX, Zhao JP (2016) Influence of radiation on predictive accuracy in numerical simulations of the thermal environment in industrial buildings with buoyancy-driven natural ventilation. Appl Therm Eng 96: 473-480
18. Arslanoglu N, Yigit A (2014) Experimental and theoretical investigation of the effect of radiation heat flux on human thermal comfort. Energ Buildings, 113: 23-29
19. Kalmár F, Kalmár T (2012) Interrelation between mean radiant temperature and room geometry. Energ Buildings 55: 414-421
20. Fu GQ, Fu JZ, Gao HL, Yao XH (2017) Squareness error modeling for multi-axis machine tools via synthesizing the motion of the axes. Int J Adv Manuf Technol 89: 2993-3008.
21. Zhou BC, Wang SL, Fang CG, Sun SL, Dai H (2017) Geometric error modeling and compensation for five-axis CNC gear profile grinding machine tools. Int J Adv Manuf Technol 92: 2639-2652
22. ISO 230–6 (2002) Test code for machine tools, part 6: determination of positioning accuracy on body and face diagonals (diagonal displacement tests). ISO

## Figure captions

**Fig. 1** Flowchart for TSMC method

**Fig. 2** Thermal radiation between surface $A_1$ and $A_2$

**Fig. 3** Sketch of machine tool and ECC

**Fig. 4** Spatial relationship between $A_1$ to $A_2$ for (a) Parallel, (b) Vertical.

**Fig. 5** (a) Geometry model. (b) Equivalent network

**Fig. 6** Machine tool topology

**Fig. 7** CAD models for (a) Schematic, (b) CFD model and (c) Finite element model.

**Fig. 8** Machine tool temperature distribution and the structure deformation with lamp radiation for (a) Temperature field ($T_1$ is 31℃ and $d_1$ is 1000 mm) and (b) Structure deformation schematic

**Fig. 9** Influence of lamp on spindle rear displacement. (a) Tool tip displacement with various $T_1$ ($d_1$ is 1000mm), (b) Tool tip displacement with various $d_1$ ($T_1$ is 46℃)

**Fig. 10** Machine tool temperature distribution and the structure deformation with ECC radiation. (a) Temperature field ($T_2$ is 21.3℃ and $d_2$ is 450mm), (b) Structure deformation schematic

**Fig. 11** Influence of ECC on spindle rear displacement. (a) Tool tip displacement with various $T_2$ ($d_2$ is 450 mm), (b) Tool tip displacement with various $d_2$ ($T_2$ is 25.3℃)

**Fig. 12** Machine tool temperature distribution and the structure deformation with pump radiation. (a) Temperature field ($T_3$ is 32℃ and $d_3$ is 1050mm), (b) Structure deformation schematic

**Fig. 13** Influence of pump station on spindle rear displacement. (a) Tool tip displacement with various T3 (d3 is 950 mm), (b) Tool tip displacement with various d3 (T3 is 38℃)

**Fig. 14** Machine tool temperature under comprehensive EHS influence for (a) Front side ad (b) Back side

**Fig. 15** Working volume and body diagonal

**Fig. 16** 21 thermal errors of machine tool for (a) Thermal errors of X axis guideway, (b) Thermal errors of Y axis guideway, (c) Thermal errors of Z axis guideway and (d) Squareness

**Fig. 17** Machine tool working volume thermal error under comprehensive EHS for (a) X directional thermal error, (b) Y directional thermal error, (c) Z directional thermal error and (d) Total thermal error

**Fig. 18** (a) Y and Z directional thermal error of path $X_1X_2$. (b) X and Z directional thermal error of path $Y_1Y_2$. (c) X and Y directional thermal error of path $Z_1Z_2$. (d) *NPP* thermal error. (e) *PPP* thermal error. (f) Total thermal error of *NPP* and *PPP*

**Fig. 19** Flowchart of experiment process

**Fig. 20** The experimental precision machine tool

**Fig. 21** Temperature and displacement points measured in the experiment. (a) Temperature sensors installed on the frontside, (b) Temperature sensors installed on the backside, (c) Non-contact capacity

**Fig. 22** EHS temperature for (a) Ambient air, (b) Lamps, ECC and HPS

**Fig. 23** Measured temperature data. (a) Column left/right sides, (b) Machine tool back sides, (c) Column front, (d) Bed

**Fig. 24** Displacements between test bar and sensors. (a) Measured displacements during all experimental process, (b) Measured displacements in 120 min, (c) Lamps caused displacements, (d) IHS caused displacements, (e) ECC caused displacements, (f) HPS caused displacements

**Fig. 25** Different heat sources effects on measured displacements variation for (a) X direction, (b) Y direction and (c) Z direction

**Fig. 26** Comparison between test and simulation for (a) Temperature of lamps experiment and simulation, (b) Temperature of ECC experiment and simulation, (c) Temperature of pump station experiment and simulation and (d) Deformation of experiment and simulation